

Magnetic mineral dissolution front delimited by late Holocene sediment accumulation acceleration in the inner shelf, northern South China Sea

Mingkun Li^{a,b,c}, Meng Tang^{c,d,*}, Liang Chen^{c,d}, Yongying Zeng^b, Rou Wen^b, Junyu Lin^b, Mingjie Yu^{b,**}

^a School of Geography, Lingnan Normal University, Zhanjiang 524048, China

^b School of Geography, South China Normal University, Guangzhou 510631, China

^c Key Laboratory of Marine Environmental Survey Technology and Application, Ministry of Natural Resources, Guangzhou 510300, China

^d South China Sea Survey Center, Ministry of Natural Resources, Guangzhou 510300, China

ARTICLE INFO

Editor: Howard Falcon-Lang

Keywords:

Environmental magnetism
Continental shelf
Human activities
Pearl River Estuary

ABSTRACT

Inner shelf sediment properties are sensitive indicators of Holocene environmental changes; however, magnetic records can be altered by reductive dissolution. To refine our understanding of magnetic mineral dissolution, we conducted detailed analyses of three sediment cores from the inner shelf of the northern South China Sea. AMS¹⁴C dating, grain-size, magnetic parameters, mineral composition, organic carbon, and sulfur content were examined. The cores, composed uniformly of clayey silt and spanning the past 4–6 ka, were divided into three zones: (1) a suboxic surface layer (40–88 cm thick), (2) an intermediate zone with moderate magnetic properties, and (3) a basal zone characterized by intense magnetic mineral dissolution. Identified minerals include magnetite, hematite, and iron-sulfide phases such as pyrite. The depth of the suboxic-sulfate boundary (Zones 1–2) was inversely correlated with sedimentation rate and water depth. The magnetic dissolution front (Zones 2–3 boundary) coincided with a sharp increase in sedimentation over the past 1–2 ka, likely linked to intensified human activity. These results suggest that anthropogenic environmental changes may have influenced magnetic mineral reductive dissolution, warranting further investigation.

1. Introduction

Marine sediments host abundant paleoenvironmental and paleomagnetic archives (e.g., Brachfeld et al., 2003; Vigliotti et al., 2008; Yang et al., 2009), and magnetic analyses have become widely used due to their efficiency, cost-effectiveness, and non-destructive nature (Ghilardi et al., 2008; Huang et al., 2018; Simkins et al., 2012; Wang et al., 2011; Zong et al., 2010). Magnetic records of terrigenous input and depositional processes, however, are susceptible to alteration via early diagenesis and the reductive dissolution of magnetic minerals such as magnetite and hematite (Canfield and Berner, 1987; Ge et al., 2015; Mohamed et al., 2011; Rowan et al., 2009; Zheng et al., 2010; Zheng et al., 2011) with the degradation of reactive organic matter in marine environment (Froelich et al., 1979; Roberts, 2015; Zhao et al., 2024). Canfield and Berner (1987) demonstrated that magnetite dissolution rates are proportional to pore water sulfide concentrations, while Karlin (1990) showed that dissolution is marked by rapid reductions in

magnetic parameters and depends on the surface area of magnetic particles. Pyrite (FeS_2), a paramagnetic product of diagenesis, typically forms at depth, leading to a downward decline in magnetic susceptibility (MS), whereas greigite, an intermediate phase of pyrite formation, may sometimes be retained in sediments (Horng et al., 1998; Roberts and Turner, 1993). Due to the ubiquity of magnetic mineral diagenesis in marine settings, magnetic signals have been employed to interpret environmental evolution (Roberts, 2015), including seabed hypoxia (Wang et al., 2025), sea level change (Liu et al., 2021a), and natural gas hydrate leakage (Badesab et al., 2019). As a result, understanding early reductive diagenesis has become a crucial focus in marine sedimentary paleoenvironment studies.

The inner shelf is particularly suitable for environmental magnetism due to its high-resolution deposits. In modern sediments, magnetic parameters are frequently used to determine sediment provenance (Ellwood et al., 2006; He et al., 2024; Kim et al., 2013; Li et al., 2024; Li et al., 2020; Wang et al., 2017; Wang et al., 2009; Xue et al., 2019) and

* Corresponding author at: South China Sea Survey Center, Ministry of Natural Resources, No. 155, Xingang West Road, Guangzhou City, 510300, China.

** Corresponding author at: School of Geography, South China Normal University, No. 55, Zhongshan Road West, Tianhe District, Guangzhou 510631, China.

E-mail addresses: tame159@qq.com (M. Tang), yunj@m.scnu.edu.cn (M. Yu).

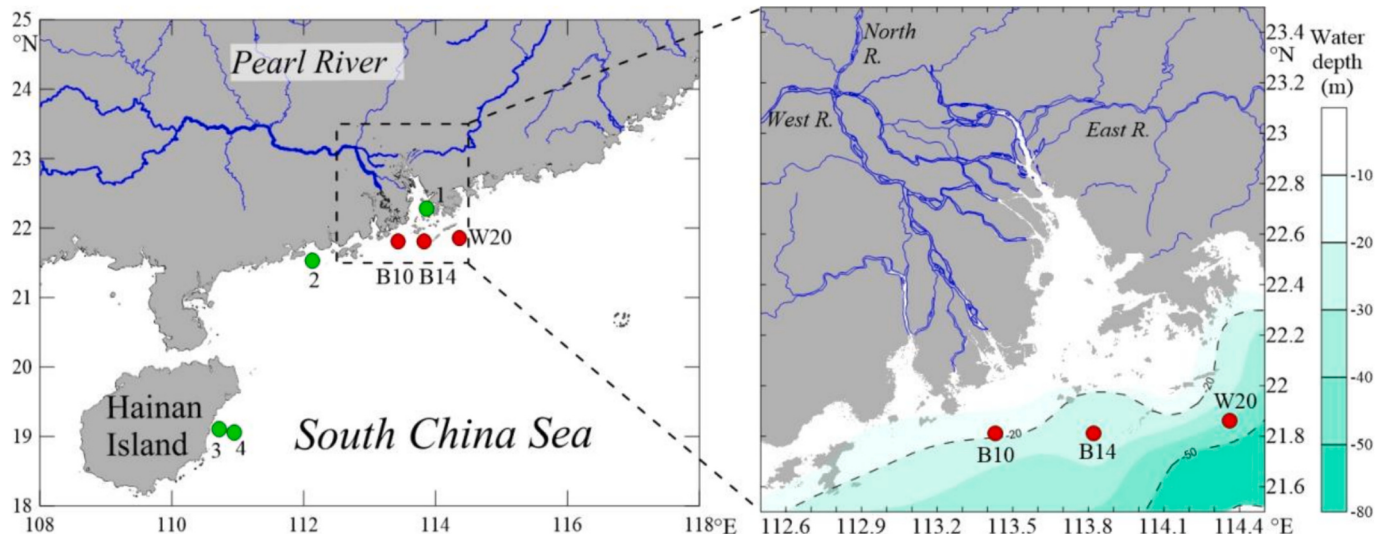


Fig. 1. Location of the study region on the northern SCS shelf and the sediment cores B10, B14, and W20. Numbers 1–4 mark the locations of cores UV1 (Zong et al., 2010), YJ (Huang et al., 2018), GH6 (Huang et al., 2021), and WC11 (Wu et al., 2024), respectively.

detect heavy metal pollution (Li et al., 2021; Wang et al., 2020). For sediment cores, magnetic properties mainly reflect terrigenous input linked to climate and anthropogenic activity in source regions (Huang et al., 2021; Huang et al., 2018; Wang et al., 2022; Wu et al., 2024). However, reduced diagenesis is also evident in some layers (Zheng et al., 2010), and its controlling factors remain poorly understood (Ge et al., 2015; Mohamed et al., 2011; Zheng et al., 2011). This uncertainty complicates the interpretation of magnetic records. Notably, in continental shelf regions near estuaries, riverine sediment fluxes have increased significantly over the Late Holocene due to intensified human activity (Jenny et al., 2019; Syvitski et al., 2022). Whether these environmental changes have influenced reductive diagenesis and magnetic mineral dissolution remains unclear.

The northern South China Sea (SCS) inner shelf (Fig. 1) offers an ideal setting to investigate this question. Previous studies (Chen et al., 2023; Xiong et al., 2020) have characterized sedimentary evolution in the Pearl River Delta and adjacent shelf. Numerous cores show downward-decreasing MS profiles consistent with magnetic mineral dissolution. Despite this, many studies attribute magnetic differences solely to terrestrial environmental change (Huang et al., 2021; Huang et al., 2018; Wu et al., 2024; Yim et al., 2004; Zong et al., 2010). For instance, Yim et al. (2004) linked elevated MS in the upper 2–3 m of cores near Hong Kong to shipping contamination. Zong et al. (2010); Huang et al. (2018, 2021) and Wu et al. (2024) associated with high MS at core tops with enhanced terrigenous input due to intensified land use. Interestingly, greigite has been reported in some northern SCS cores (Ouyang et al., 2013), though the detailed magnetic analysis are lacking.

In this study, we employ high-resolution environmental magnetic, mineralogical, and chronological methods to investigate the link between sediment accumulation and diagenesis. We find that magnetic transformations commonly occur during periods of increased accumulation, indicating a relationship between diagenesis and basin environment evolution. This newly identified phenomenon provides an indirect approach to investigating reductive diagenesis and the Fe-C-S cycle.

2. Materials and methods

2.1. Regional settings

The northern inner shelf of the SCS, particularly the area adjacent to the Pearl River Estuary (PRE) (Fig. 1), serves as an important sedimentary archive for reconstructing Holocene paleoenvironmental

Table 1
Basic information of the three study cores.

Core ID	Water depth (m)	Core length (m)	Location
B10	26.8	3.40	113.43°E, 21.81°N
B14	33.2	3.14	113.82°E, 21.84°N
W20	46.8	3.12	114.36°E, 21.86°N

evolution. The Pearl River consists of the West (*Xijiang*), North (*Beijiang*), East (*Dongjiang*) Rivers, along with several smaller tributaries in the Pearl River Delta. Geologically, the source region in southern China is primarily composed of Mesozoic granitic rocks (mainly Cretaceous and Jurassic), Devonian to Triassic carbonates, and Cenozoic sedimentary rocks (Wang et al., 2016). Geomorphologically, the Pearl River Basin is dominated by mountainous and hilly terrain, interspersed with small and scattered plains. The northwestern portion comprises the Yunnan-Guizhou Plateau, which has an average elevation of 1000–2000 m and contains numerous a group of basins and lakes, while the eastern part is a low mountain and hilly area, with an altitude of around 500 m. Climatically, the Pearl River Basin experiences a subtropical to tropical maritime monsoon climate (An, 2000). The modern mean annual temperature is approximately 22 °C, and average annual precipitation ranges from 1600 to 2000 mm. More than 80 % of the annual rainfall occurs during spring and summer, resulting in warm, humid summers and cool, dry winters (Zong et al., 2009).

Surficial sediments in the study area offshore of the PRE has been dominated by Pearl River-derived mud deposits since the middle Holocene, in addition to residual sand from the Late Pleistocene (Liu et al., 2014; Wang et al., 2023; Zhong et al., 2017). These mud deposits primarily cover the continental shelf in water depths shallower than 90 m, extending from the PRE to Hainan Island. This distribution is driven by the high sediment supply and westward transport by coastal current. In contrast, it is difficult to receive the Pearl River-supplied mud in the deep water area (Wang et al., 2023).

2.2. Sampling

Three sediment cores (B10, B14, and W20) were recovered using gravity coring during a 2022 cruise by the South China Sea Survey Center, Ministry of Natural Resources (Fig. 1). Basic information for each core is listed in Table 1. Upon recovery, the plastic core tubes were split longitudinally along the central axis using an electric saw. Each

Table 2

Magnetic parameters measured in this study and their definitions (after Maher (2007); Oldfield (1991)).

Magnetic parameter	Abbreviation/ Symbol	Interpretation
Low-frequency dependent magnetic susceptibility	χ_{lf}	Indicates the total magnetic mineral concentration, including both low-coercivity ferrimagnetic minerals (e.g., magnetite and maghemite) and high-coercivity magnetic/anti-ferromagnetic minerals (e.g., hematite and goethite) with various domain states (superparamagnetic, single domain, "pseudo-single domain," and multidomain).
Saturation isothermal remanent magnetization	SIRM	Reflects the concentration of remanence-carrying magnetic minerals, independent of superparamagnetic grains.
Anhysteretic remanent magnetization	ARM	Proportional to the concentration of stable single domains (SSD) ferrimagnetic grains.
Ratio of susceptibility of ARM to χ_{lf}	χ_{ARM}/χ_{lf}	Indicator of magnetic mineral grain size. Higher values suggest a greater proportion of SSD grains.
Ratio of SIRM to χ_{lf}	SIRM/ χ_{lf}	Reflects both the grain size and type of magnetic minerals.
Ratio of ARM to SIRM	ARM/SIRM	Another proxy for magnetic grain size. Higher values indicate a greater concentration of SSD grains.
Frequency-dependent magnetic susceptibility "Hard" isothermal remanent magnetization	χ_{fd}	Indicates the concentration of ultra-fine magnetic grains (mainly superparamagnetic particles).
"Hard" isothermal remanent magnetization	HIRM	Represents the absolute concentration of high-coercivity minerals, such as hematite and goethite.
S_{-300}	S_{-300}	Ratio of low-coercivity (e.g., magnetite, maghemite) to total remanence-carrying minerals (SIRM). A high S_{-300} (close to 1) indicates dominance of low-coercivity minerals, while a low value (close to 0) reflects a higher content of high-coercivity minerals (e.g., hematite and goethite).

core was then further divided into two halves with a nylon thread. In their moist state, the three cores were visually homogeneous and composed predominantly of bluish-gray silt. In addition, shell fragments with diameters of 1 to 2 cm were observed in core B10 at depths of 27 cm and 305 cm, in core B14 at 131 cm and 142 cm, and in core W20 at 278 cm. Half of each core was subsampled by vertically inserting nonmagnetic plastic cubes ($2 \times 2 \times 2 \text{ cm}^3$) into the fresh, wet sediment throughout the entire core length. Samples were collected at 2 cm intervals, yielding 170, 157, and 156 samples from the cores B10, B14, and W20, respectively. Parallel subsamples for grain size and geochemical analyses were taken from the same depth intervals.

2.3. Chronology

A total of 14 accelerator mass spectrometry (AMS) radiocarbon (^{14}C) dating samples were selected from the three studied cores. These included nine samples of foraminifera (*Globigerinoides Ruber*) and five complete shell samples. The analyses were conducted at the Guangzhou Institute of Geochemistry, Chinese Academy of Sciences. Radiocarbon ages were calibrated using OxCal v4.4.4 (<https://c14.arch.ox.ac.uk/oxcal/OxCal.html>), with the Marine20 calibration curve applied. A regional reservoir correction age (ΔR) of 18 ± 37 years was used, based on the average of three nearby SCS sites in the Marine Reservoir Correction Database (<http://intcal.qub.ac.uk/calib/>). Bayesian age-depth modeling was carried out using the R programming environment and Bacon v2.2 package (Blaauw and Christen, 2011). Sediment deposition rates (SR) were calculated from depth and age intervals using

the formula:

$$\text{SR} = \text{core depth interval}/\text{age interval} \quad (1)$$

Based on the established chronological framework, dry density (DD) and sediment accumulation rate (SAR) were also carried. DD was determined by weighing freeze-dried cubic samples ($2 \times 2 \times 2 \text{ cm}^3$) using an analytical balance and dividing the mass (W) by the sample volume (V). SAR was then derived by multiplying DD by SR. The calculation formulas are as follows.

$$\text{DD} = W/V \quad (2)$$

$$\text{SAR} = \text{DD} \times \text{SR} \quad (3)$$

2.4. Grain-size analysis

Grain-size analyses were conducted on 212 subsamples collected at approximately 10 cm intervals from the three sediment cores. Each subsample (<1 g dry weight) underwent chemical pretreatment. Organic matter was oxidized using 30 % hydrogen peroxide (H_2O_2), followed by the removal of carbonate minerals through dissolution in 5 M hydrochloric acid (HCl). Digestion was monitored by periodic stirring with a glass rod at six-hour intervals, and completion was confirmed by the absence of gas evolution, typically requiring 24 h. Triplicate measurements of each pretreated sample were conducted using a Malvern Mastersizer 3000 laser diffraction particle analyzer (Malvern Panalytical, UK) to ensure analytical precision.

2.5. Magnetic measurements

Magnetic measurements included both magnetic parameters (magnetic susceptibilities and remanent magnetization) (Table 2) and thermal dependence of MS ($\kappa\text{-T}$).

Volumetric low- and high-frequency dependent MS (κ_{lf} and κ_{hf}) were measured at 976 Hz and 15,616 Hz, respectively, under a low field (200 m/A) using a Kappabridge MFK1-FA (AGICO, Czech Republic). These values were converted to mass susceptibilities (χ_{lf} and χ_{hf}) by dividing by sample density. Frequency-dependent MS (χ_{fd}) was calculated as:

$$\chi_{fd} = (\chi_{lf} - \chi_{hf})/\chi_{lf} \quad (4)$$

χ_{fd} reflects the concentration of the ultra-fine magnetic particles near the boundary between superparamagnetic (SP) and single domain (SD) behavior (Stephenson, 1971; Oldfield, 1991).

Anhysteretic remanent magnetization (ARM) was imparted using an alternating field of 100 mT combined with a 0.05 mT direct current (DC) bias, applied with an LDA5 demagnetizer (AGICO, Czech Republic). ARM, representative of stable single-domain (SSD), was measured with a JR-6 Spinner Magnetometer (AGICO, Czech Republic) (Oldfield, 1991). The ARM was measured using a JR-6 Spinner Magnetometer (AGICO, Czech Republic). Magnetic susceptibility of ARM (χ_{ARM}) was calculated by dividing the ARM by the DC bias field. Saturation isothermal remanent magnetization (SIRM) was imparted to the Z-axis for each sample at a DC field of 2 T using a DMP1 Pulsed magnetometer (EUSCI, China), and measured using the JR-6 Magnetometer. SIRM primarily reflects the concentration of ferrimagnetic minerals and is unaffected by SP grains. However, they are irrelevant to superparamagnetic domains. Isothermal remanent magnetization under a back field of -300 mT ($\text{IRM}_{-300\text{mT}}$) was also measured to determine the S-ratio (S_{-300}):

$$S_{-300} = -\text{IRM}_{-300\text{mT}}/\text{SIRM} \quad (5)$$

S_{-300} is a proxy for the proportion of low- versus high-coercivity magnetic minerals. Higher values indicate dominance of low-coercivity minerals such as magnetite and maghemite (Bloemendal et al., 1993).

Complementary $\kappa\text{-T}$ analyses were conducted on parallel aliquots using the MFK1-FA Kappabridge equipped with a CS4 high-temperature

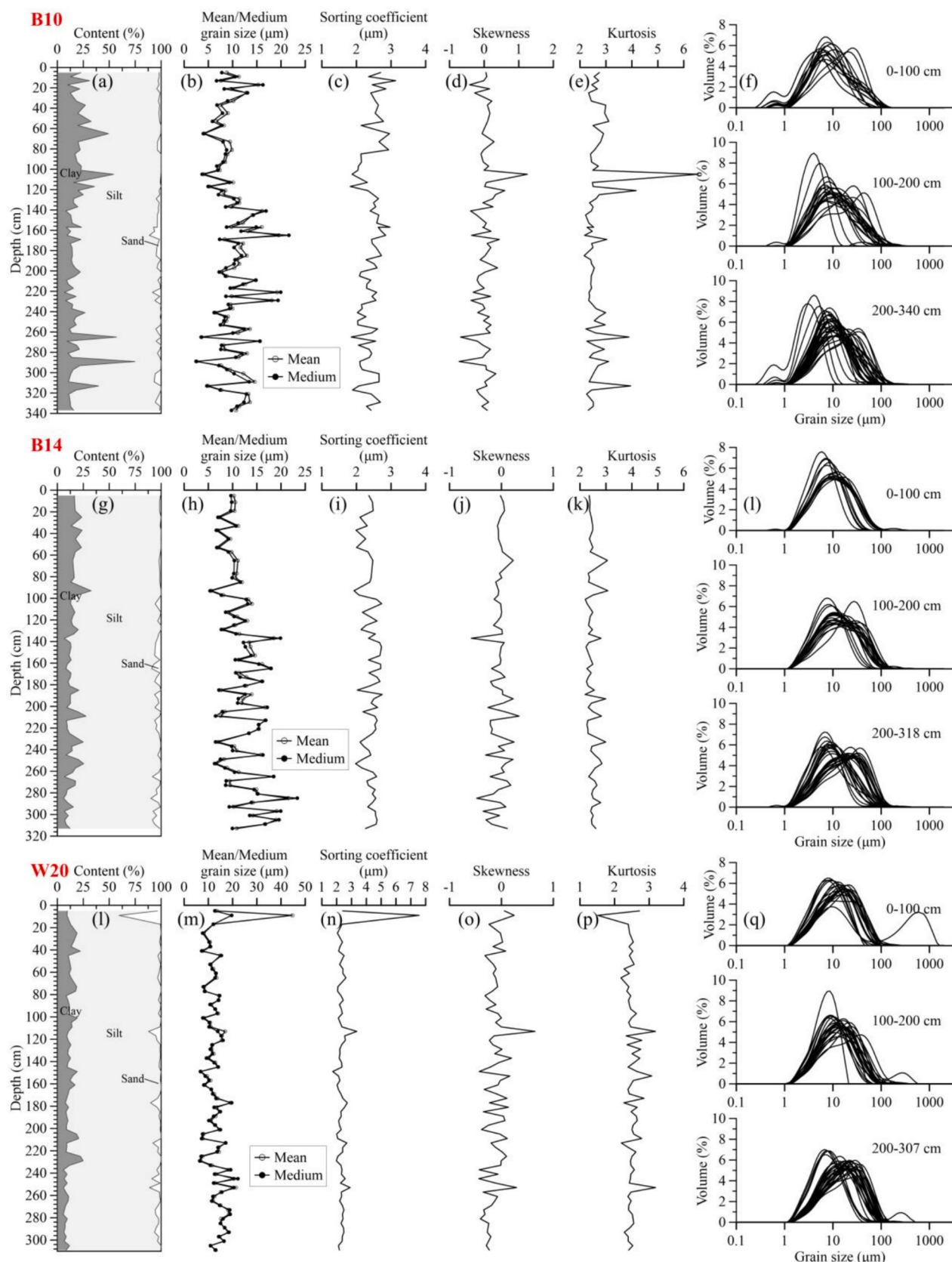


Fig. 2. Down-core variations in grain-size parameters for cores B10, B14, and W20: (a, g, l) clay-silt-sand components, (b, h, m) mean and medium grain sizes, (c, i, n) sorting coefficient, (d, j, o) skewness, (e, k, p) kurtosis, and (f, l, q) grain-size distribution curves.

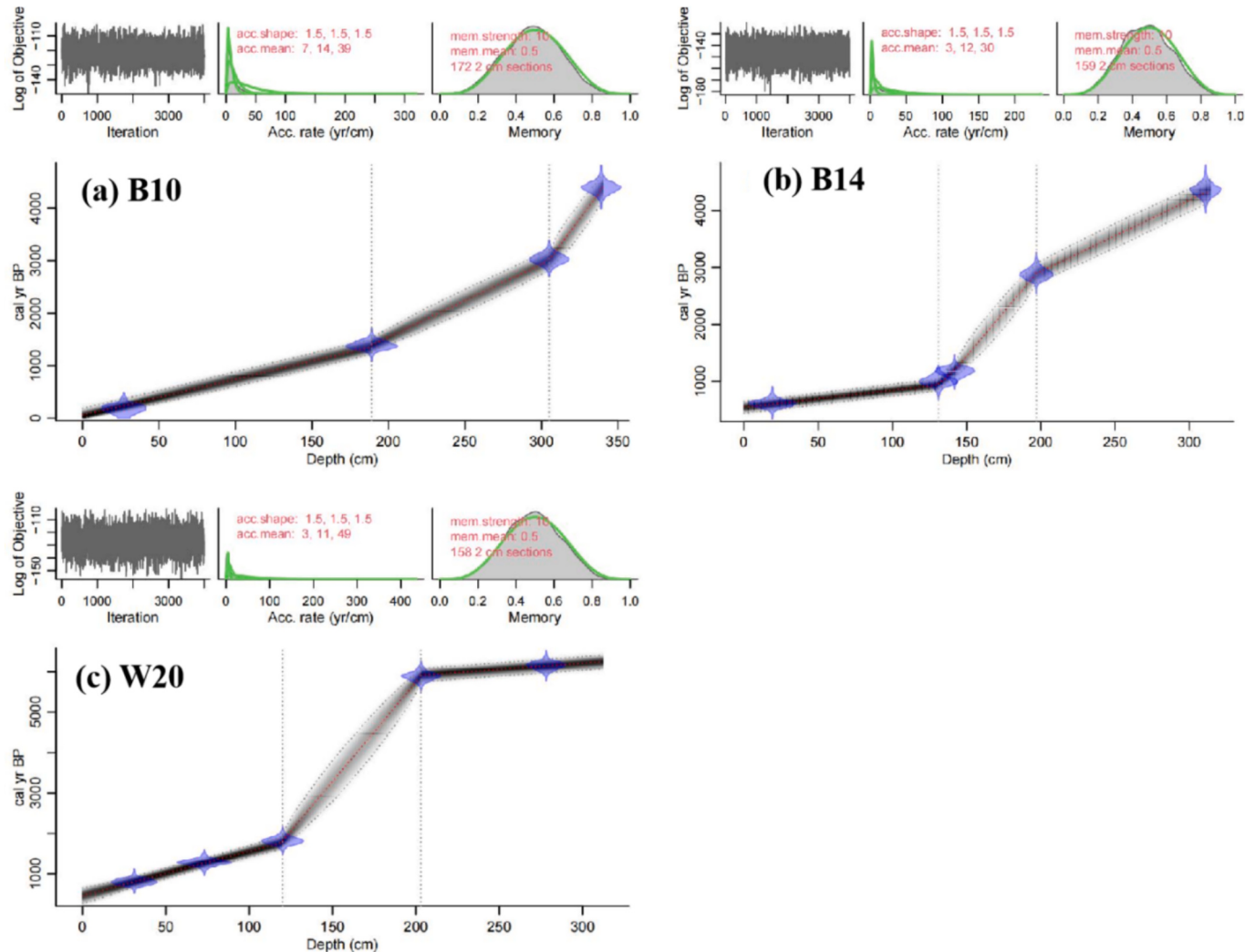


Fig. 3. Age-depth models of cores (a) B10, (b) B14, and (c) W20 based on AMS¹⁴C dating and Bacon modeling.

furnace (AGICO, Brno, Czech Republic). Magnetic susceptibility (κ) was recorded as a function of temperature during continuous heating and cooling between 40 and 700 °C at a controlled rate of 5 °C/min under an argon atmosphere.

2.6. SEM-EDS tests for magnetic minerals

Magnetic mineralogical characterization was performed through integrated microscopic and geochemical analysis. Ferrimagnetic concentrates were physically extracted from six representative samples, with two selected from each core corresponding to relatively high and low magnetic susceptibility intervals. The concentrates were separated using hand-held magnets and further purified by gravimetric separation in anhydrous ethanol. Carbon-coated subsamples were analyzed using a FEI Quanta 650 FEG scanning electron microscope (SEM, Thermo Fisher Scientific, USA) equipped with an Oxford Instruments X-Max 80 energy-dispersive spectroscopy (EDS) detector (Abingdon, UK). SEM-EDS observations were conducted under high vacuum conditions ($\sim 10^{-3}$ Pa) at an accelerating voltage of 15 kV. A total of 322 magnetic grains were identified across all samples. Triplicate elemental mappings were acquired for each specimen, focusing on Fe-Ti-Cr spinels and iron sulfides. Quantitative EDS results were normalized against NIST-traceable calibration standards (SRM 470), achieving less than 2 % atomic ratio uncertainty using ZAF matrix correction algorithms.

2.7. TOC and TS measurements

Thirty samples from the three sediment cores were analyzed for total organic carbon (TOC) and total sulfur (TS). The procedure consisted of three sequential steps. First, oven-dried sediment samples were ground with an agate mortar to a grain size finer than 200 mesh (<75 µm). Inorganic carbon was then removed using a vapor-phase acid digestion technique: 30 % hydrochloric acid was placed in the base of a sealed reaction vessel, while the sediment sample was suspended in the middle chamber. The setup maintained exposure to HCl vapor for 48 h, with periodic acid replenishment to ensure complete carbonate decomposition. Following acid treatment, approximately 100 mg of each sample was mixed with a combustion flux and analyzed using an Eltra CS800 carbon/sulfur analyzer. The system is equipped with a high-frequency induction furnace operating at 1450 °C and an infrared detection unit. Measurements followed manufacturer-specified calibration protocols for simultaneous TOC and TS quantification.

3. Results

3.1. Lithology

All three sediment cores are primarily composed of homogeneous clayey silt (Fig. 2), with grain-size composition generally comprising 10–15 % clay and 70–80 % silt. Sand content remains below 10 % in

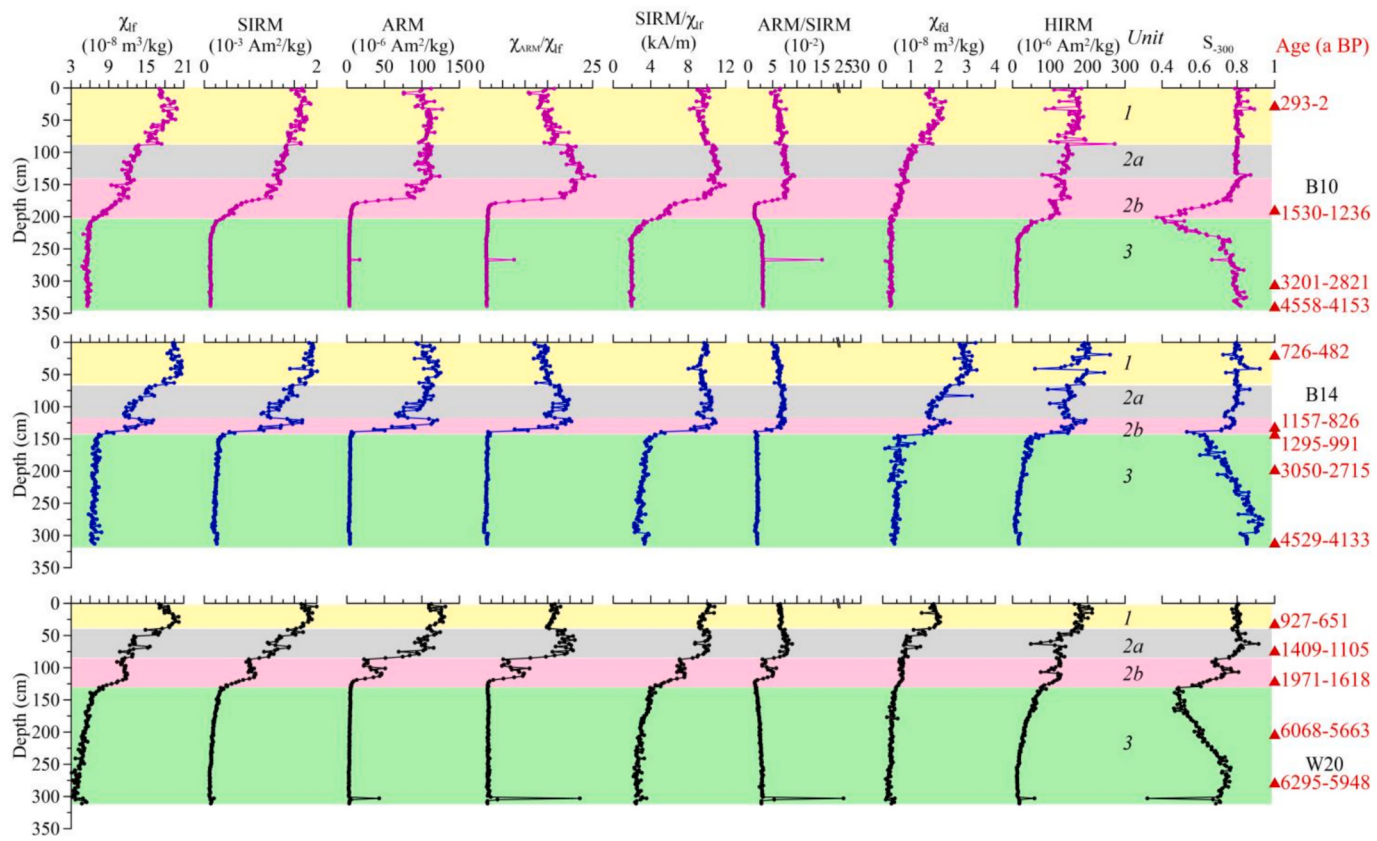


Fig. 4. Down-core variations in magnetic parameters of cores B10, B14, and W20.

most intervals, except for isolated horizons in core W20 where sand exceeds 10 % ($n = 1$). Mean and medium grain sizes for most samples range from 5 to 20 μm , with coarser layers occurring at approximately 170 cm and 220 cm in B10, 280 cm in B14, and 10 cm in W20 (Fig. 2b, h, m). Sorting coefficients for all samples are within 2–3 μm , except at the 10 cm level of W20, which shows greater variability (Fig. 2c, i, n). Skewness values fall between –1 to 1 (Fig. 2d, j, o), and kurtosis values mostly range from 1 to 3, with anomalously high values observed between 100 and 120 cm in B10 (Fig. 2e, k, p). Most grain-size distributions exhibit a single mode centered in the silt fraction (Fig. 2f, l, q). Overall, the consistent lithology and grain-size distributions suggest stable sedimentary hydrodynamic conditions during deposition.

3.2. Chronology

All three cores display well-preserved chronological sequences. Bayesian age-depth models generated using the Bacon software constrain the basal ages to 4353 cal yr BP (B10), 4343 cal yr BP (B14), and 6250 cal yr BP (W20) (Fig. 3). Sedimentation rates (SR) range from 0.025 to 0.17 cm/a in B10, 0.03 to 0.4 cm/a in B14, and 0.02 to 0.4 cm/a in W20. Corresponding mass accumulation rates (SAR) vary between 0.01 and 0.09 g·cm⁻²·a⁻¹ for B10, 0.02 and 0.25 g·cm⁻²·a⁻¹ for B14, and 0.01 and 0.32 g·cm⁻²·a⁻¹ for W20. All cores exhibit a clear upward increase in both SR and SAR, suggesting a progressive enhancement of sediment supply over time.

3.3. Down-core variations in magnetic parameters

Down-core variations in magnetic parameters allow identification of three distinct zones with different magnetic properties in all three studied cores (Fig. 4). Notable excursions in ARM at approximately 250 cm in core B10 and 300 cm in core W20 appear to be anomalies and were excluded from the classification of zones.

3.3.1. Zone 1

The uppermost layers, ranging from 40 to 88 cm, in all three cores exhibit the highest average values of concentration-dependent magnetic parameters, including χ_{if} , SIRM, ARM, χ_{fd} , and HIRM (Fig. 4). In this zone, the average S_{-300} value is approximately 0.8, which is higher than in the underlying layers (Fig. 4). The ratios $\chi_{\text{ARM}}/\chi_{\text{if}}$, ARM/IRM, and SIRM/ χ_{if} are relatively consistent and show a decreasing trend toward the surface (Fig. 4).

3.3.2. Zone 2

Located below Zone 1, Zone 2 is defined as a transition layer marked by a pronounced decline in χ_{if} from its maximum to minimum values. This layer is also characterized by substantial and systematic changes in magnetic parameters (Fig. 4). Zone 2 is subdivided into two parts, labeled 2a and 2b. In Zone 2a, there is a sharp decrease in concentration-dependent magnetic parameters, including χ_{if} , SIRM, ARM, χ_{fd} , and HIRM. Parameters such as χ_{if} , SIRM, which are more sensitive to coarser grains in the multi-domain and pseudo-single-domain range, show the most rapid decreases (Fig. 4). At the same time, the ratios $\chi_{\text{ARM}}/\chi_{\text{if}}$, ARM/IRM, and SIRM/ χ_{if} increase abruptly, indicating a relative enrichment of fine-grained stable single-domain particles.

This shift may reflect the preferential loss of coarse particles or the formation of finer grains through diagenesis. The gradual decline in HIRM, along with only minor changes in S_{-300} (Fig. 4), suggests that high coercivity minerals are becoming less abundant but are more resistant to dissolution compared to magnetite.

In Zone 2b, a secondary peak in concentration-dependent magnetic parameters is followed by a rapid downward decrease (Fig. 4). Both HIRM and S_{-300} also decrease (Fig. 4), indicating enhanced dissolution of high coercivity minerals such as hematite. A noticeable reduction in the ratios $\chi_{\text{ARM}}/\chi_{\text{if}}$, ARM/IRM, and SIRM/ χ_{if} compared with Zone 2a suggests grain coarsening, likely caused by the loss of fine-grained magnetic minerals due to strong reductive dissolution.

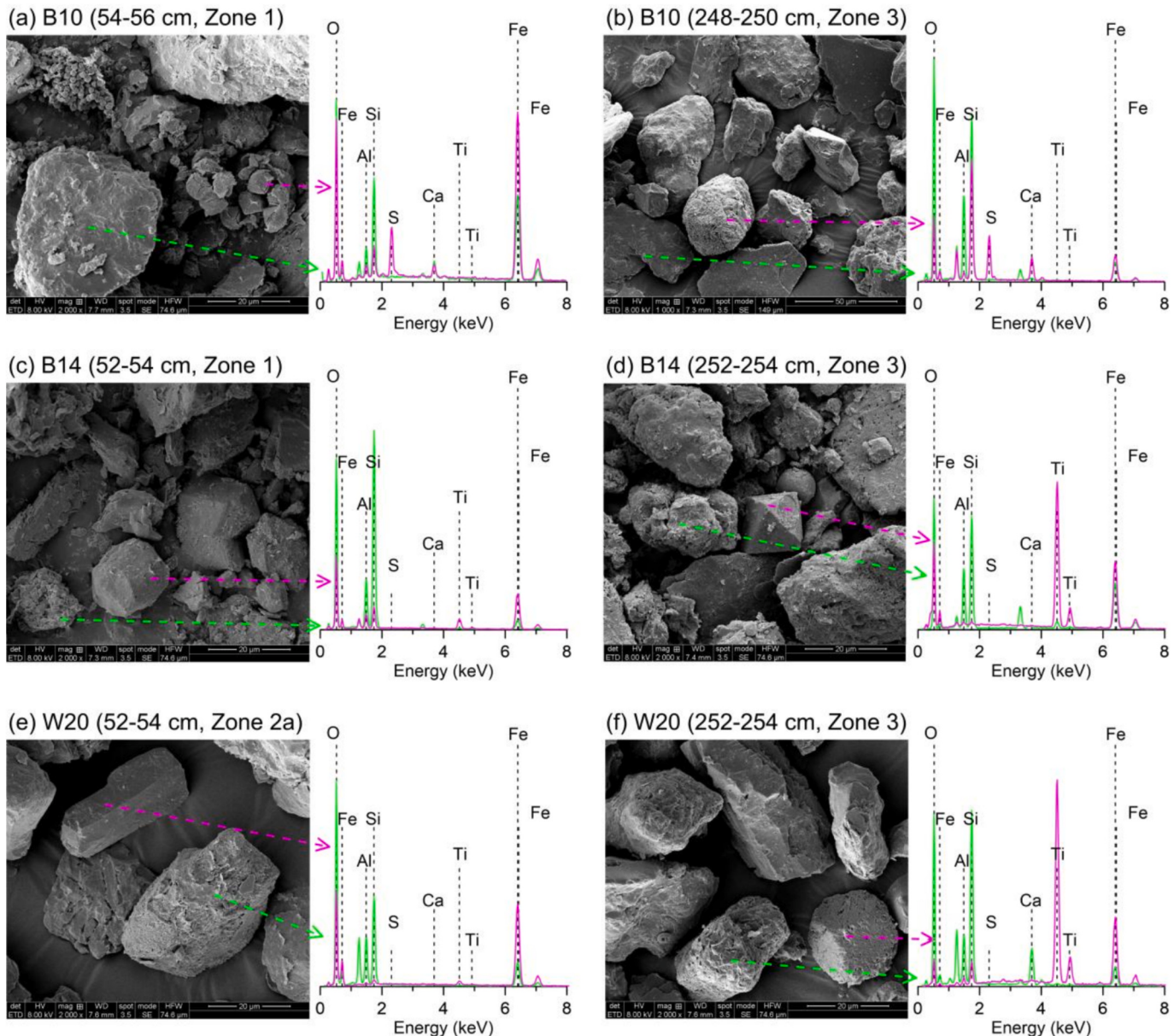


Fig. 5. Scanning electron microscope images (secondary electron) of magnetic mineral extracts from different sediment zones in cores B10, B14, and W20.

3.3.3. Zone 3

The lowermost section of each core is defined as Zone 3. This zone is characterized by significantly reduced magnetic signals. All concentration-dependent magnetic parameters fall to approximately 10 to 20 % of their respective averages in Zone 1 (Fig. 4). This reduction is less apparent in the SIRM and χ_{lf} profiles, but more prominent in the ARM profile (Fig. 4), indicating an increased presence of magnetic grains within the single-domain size range near the core base. Most parameters in this zone remain stable except for S_{-300} . A clear increase in S_{-300} is observed with depth, rising from 0.4 to values between 0.8 and 0.9. This trend suggests that high coercivity minerals contribute progressively less to the overall magnetic signal in the deeper sediment layers.

3.4. Magnetic minerals

Magnetic mineral analysis was conducted on selected samples from Zone 1 and Zone 3 of cores B10 and B14, and from Zones 2b and 3 of core W20. SEM observations revealed that most extracted magnetic particles

range in size from 10 to 50 µm (Fig. 5). Sub-rounded, flake-shaped, rod-like, and other irregular particle morphologies were commonly observed (Fig. 5). Damaged rhombic octahedral structures were also found (Fig. 5c, d, f).

Energy-dispersive spectroscopy (EDS) data indicated that Fe, Ti, O, Si, S, and Ca are the dominant elements in most samples. Sulfur signals were prominent in samples from Zones 1 and 3 of core B10, while titanium signals were more pronounced in samples from cores B14 and W20. These results suggest that iron oxides and iron sulfides are likely the dominant magnetic minerals present. Rhombic octahedral and irregular particles were likely composed of (titano)magnetite, which is commonly found in marine sediments (Fig. 5a-f) (Badesab et al., 2019). In core B10, strawberry-shaped (Fig. 5a) and irregular (Fig. 5b) iron sulfides were also identified, which may represent pyrite or colloidal pyrite.

3.5. Thermomagnetic curves

Thermomagnetic (κ -T) analyses provided critical insights into

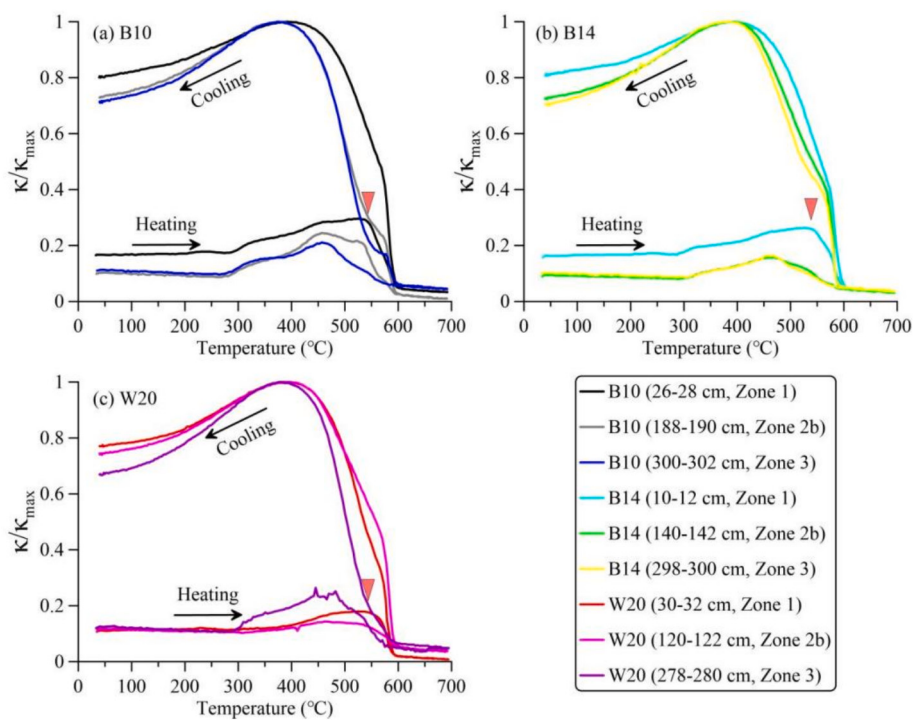


Fig. 6. Temperature dependence of magnetic susceptibility ($\kappa - T$) for representative sediment samples.

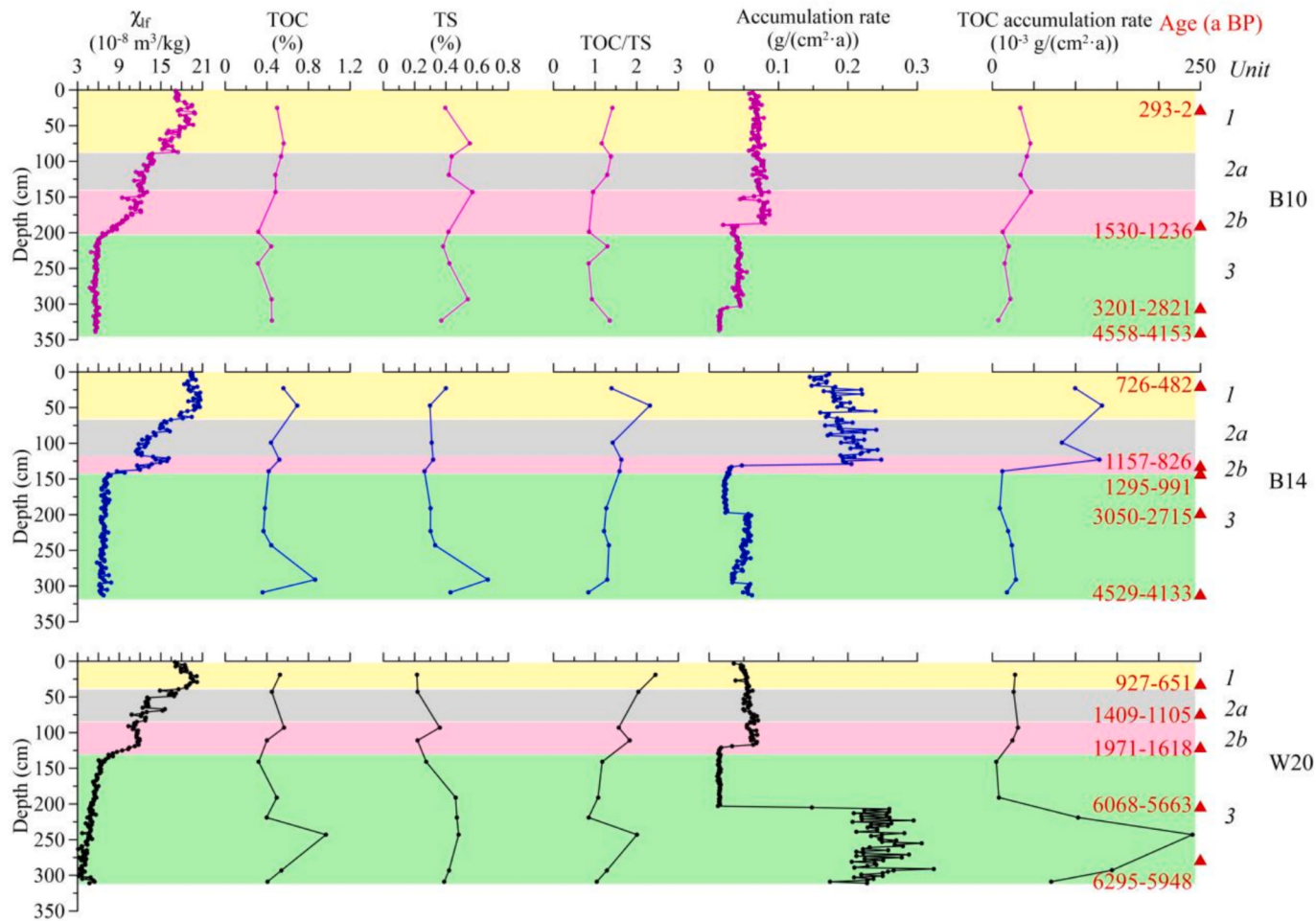


Fig. 7. Down-core variations in χ_{lf} , TOC, TS, TOC/TS ratio, accumulation rate, and TOC accumulation rate in cores B10, B14, and W20.

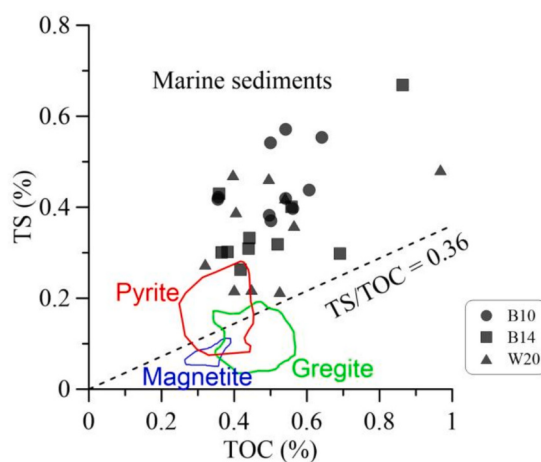


Fig. 8. Scatter plot of TS versus TOC for the studied sediments. The line representing a TS/TOC ratio of 0.36 corresponds to the value for typical marine sediments (Berner, 1982). The colored fields delineating pyrite, greigite, and magnetite are based on empirical summaries by Kao et al. (2004).

magnetic mineral assemblages (Dunlop and Özdemir, 2001). All heating curves exhibited four diagnostic transitions (Fig. 6). First, magnetic susceptibility (κ) increased gradually up to 280 °C, likely due to the unblocking of fine magnetic grains near the superparamagnetic to single-domain (SP/SD) threshold (Ge et al., 2015). Second, a pronounced enhancement in κ occurred between 250 and 350 °C, which likely reflects oxidation-induced phase transitions from metastable iron sulfides and clayey minerals into magnetite (Dunlop and Özdemir, 2001; Maher and Thompson, 1999). Third, a marked decrease in κ to near-zero values was observed around 585 °C, corresponding to the Curie temperature (Tc) of magnetite. Fourth, the cooling branches displayed κ values that were three to five times higher than those during initial heating, indicating substantial neoformation of ferrimagnetic minerals during thermal cycling (Passier et al., 2001).

There were clear differences between samples from Zone 1 and those from Zones 2 and 3 (Fig. 6). In Zone 1, κ peaks occurred at approximately 550 °C (marked by red triangles in Fig. 6), whereas in Zones 2 and 3, the peaks were observed at 450 to 500 °C. In general, the gradual κ enhancement from 250 to 550 °C is associated with the transformation of goethite into ferrimagnetic minerals such as magnetite, especially in environments with organic carbon and calcium carbonate (Hanesch et al., 2006). In contrast, κ peaks at 450 to 500 °C are typical for greigite and pyrite-bearing sediments (Duan et al., 2017). These findings suggest that Zone 1 is dominated by Fe—O minerals, while Zones 2 and 3 contain relatively higher concentrations of Fe—S minerals.

3.6. Features of TOC, TS, TOC/TS ratio, and accumulation rates

The geochemical and sedimentological analyses revealed three major findings (Fig. 7).

- (1) Across all three cores, TOC concentrations ranged from 0.3 % to 1.1 % and exhibited synchronous variations with TS content, which ranged from 0.2 % to 0.7 %. These values yielded TOC/TS ratios of approximately 1 to 3. Stratigraphic profiles showed contrasting vertical trends: TOC was depleted in the middle sections and enriched in both the upper and lower parts of the cores. In contrast, TS showed progressive enrichment with depth. This inverse relationship resulted in a consistent increase in TOC/TS ratios from bottom to top.
- (2) Sediment mass accumulation rates (MAR) ranged from 0.01 to 0.32 g/(cm²·a), with the highest value found in the basal section of core W20. The MAR profiles displayed an upward increase,

with Zone 2b marking a key transition from low background accumulation to enhanced modern sedimentation.

- (3) TOC accumulation rates closely followed the trends observed in MAR profiles, despite resolution limitations. These rates increased consistently upward, except in the basal section of core W20, where unusually high MAR coincided with exceptionally elevated TOC accumulation.

In all measured samples, relatively high TS values and low TOC concentrations resulted in TS/TOC ratios greater than 0.36. The TOC versus TS serves as an empirical tool for discriminating between mineral types and organic matter sources. According to the classification criteria shown in Fig. 8, the organic matter in the three studied cores is predominantly of marine origin, with most data points falling within the field associated with pyrite formation.

4. Discussions

4.1. Input and dissolution of magnetic minerals

Based on two lines of evidence, the magnetic variation patterns observed in the three studied cores conform to the classic model of magnetic mineral diagenesis and dissolution (Badesab et al., 2019; Mohamed et al., 2011; Roberts, 2015; Rowan et al., 2009; Zheng et al., 2010; Zheng et al., 2011). First, in Zones 2 and 3, concentration-dependent magnetic parameters such as χ_{lf} , SIRM, and ARM show substantial reductions (Fig. 4). In particular, ARM values are lowest in Zone 3, indicating significant depletion of stable single-domain (SSD) magnetite. Additionally, the lowest S_{-300} suggests a shift in mineral assemblages, with higher proportions of high coercivity minerals such as hematite and goethite relative to low-coercivity minerals like magnetite (Fig. 4). These patterns are consistent with a diagenetic environment where oxygen depletion initiates reducing conditions near the base of the sediment column (Hesse and Stoltz, 1999). As sulfate reduction progresses, iron oxides are gradually dissolved, and pyrite begins to form near the sediment base. In some cases, if the diagenetic process is incomplete or restricted, greigite may be preserved as an intermediate phase (Roberts, 2015). Notably, SSD magnetite is more readily dissolved under reducing conditions, whereas goethite and hematite are more strongly resistant to diagenesis (Hilgenfeldt, 2000). Second, Fe—S minerals are abundant in Zones 2 and 3. Although the presence of greigite cannot be definitively confirmed, the TOC and TS relationship shown in Fig. 8 suggests extensive diagenetic alteration, resulting in the widespread formation of pyrite. The absence of clearly identified greigite may reflect its instability under the prevailing sedimentary conditions or the limited number of samples analyzed for magnetic mineralogy.

Despite the varying degrees of reductive dissolution that altered the magnetic mineral assemblages in the lower zones, the uppermost layers (Zone 1) preserve magnetic signatures of detrital origin. These signatures are consistent with source characteristics and remain relatively unaffected by early diagenesis. Previous research has identified three distinct magnetic provinces in the Pearl River Estuary and northern SCS shelf system (Fig. 9). These include: (1) a western mud-dominated high-susceptibility area influenced by fine-grained sediments from the West River (Region A) (Liu et al., 2010; Zhong et al., 2017), (2) an eastern transitional zone with mixed provenance at the eastern part of the estuary (Region B); and (3) an outer shelf low-susceptibility area representing distal fluvial deposition (Region C) (He et al., 2024; Li et al., 2024; Ouyang et al., 2017). The three cores in this study are located in Region C. Magnetic parameters from Zone 1 in all three cores, including χ_{lf} , SIRM, ARM, χ_{fd} , χ_{ARM}/χ_{lf} , S_{-300} , and χ_{ARM}/χ_{lf} , closely match those observed in Region C (Table 3). Both concentration-dependent parameters (χ_{lf} , SIRM, ARM, χ_{fd} , HIRM) and S_{-300} in Zone 1 fall within the expected range for this region (Table 3, Fig. 9). However, χ_{ARM}/χ_{lf} and S_{-300} values for a sample lie outside the regional range. These two

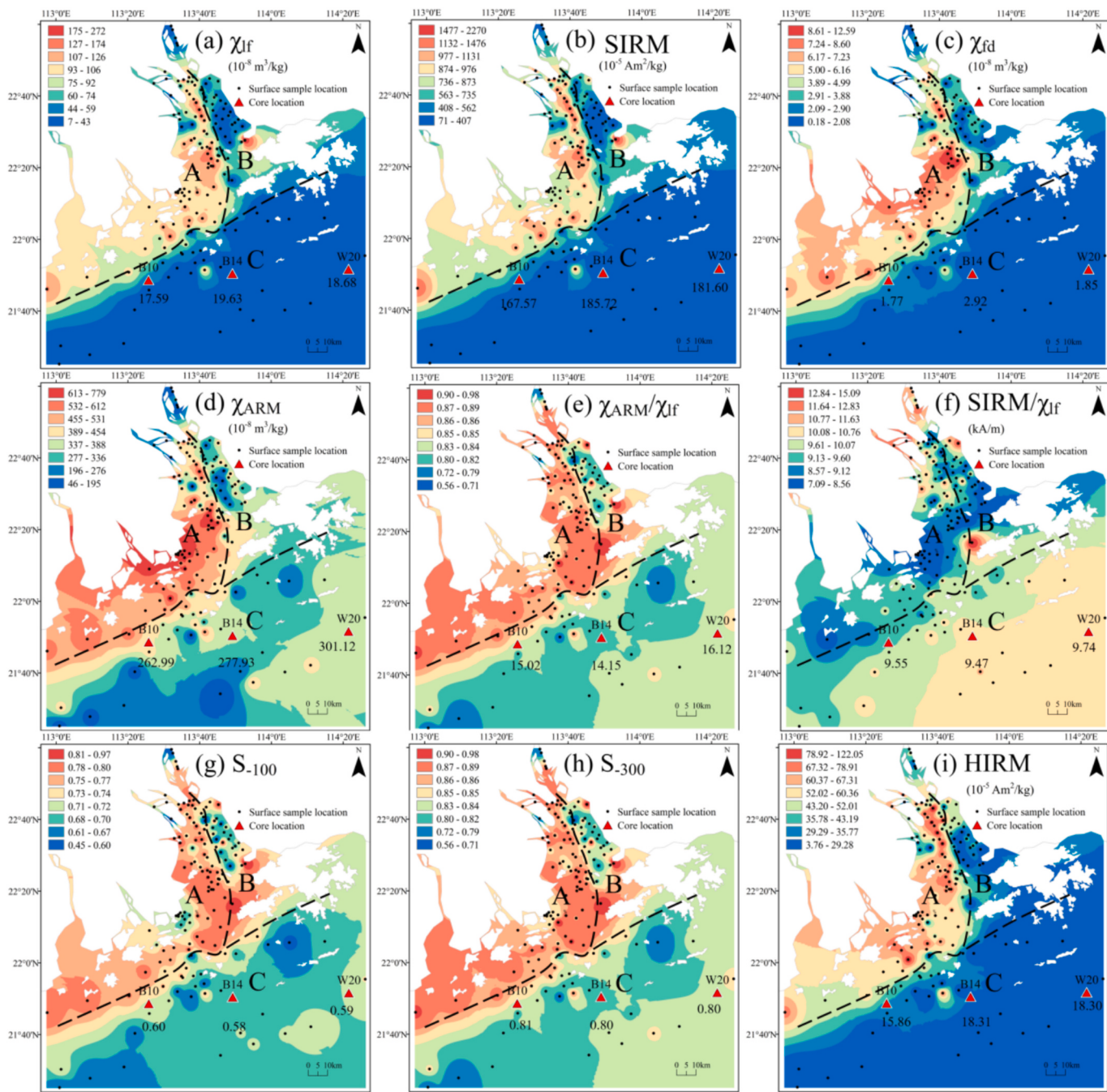


Fig. 9. Comparisons of magnetic parameters between Zone 1 in the three studied cores (numbers marked in figures) and surface sediment provinces identified in previous studies (Li et al., 2024).

ratios are known to be sensitive to grain size variations (Li et al., 2017), and the observed deviations may reflect local hydrodynamic influences.

In summary, the magnetic properties of the Zone 1 reflect detrital input and hydrodynamic sorting, while magnetic signatures in Zones 2 and 3 are substantially altered by diagenetic dissolution. Therefore, the inner shelf sediment cores preserve both signals of terrestrial magnetic mineral input and post-depositional transformation.

4.2. Updated model for magnetic mineral dissolution in continental shelves

The boundary between Zones 1 and 2, defined as the suboxic-sulfate boundary (SSB), reflects key geochemical processes, including the

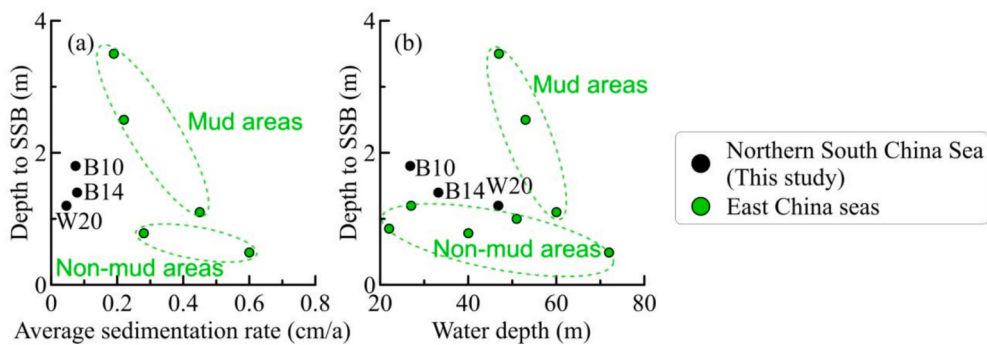
consumption of organic carbon and sulfate formation in sediments. This boundary has attracted considerable attention. In the Ria de Vigo, a fjord in the northwest Iberian Peninsula, the SSB depth ranges from 3 to 40 cm (Mohamed et al., 2011). In the inner shelf of the East China Seas, SSB depths range from 49 to 350 cm (Ge et al., 2015; Zheng et al., 2011). In this study, SSB depths in the northern SCS shelf are consistent with those in the East China Sea. Zheng et al. (2011) proposed that SSB depth is negatively correlated with the average sedimentation rates in East China Sea shelf cores (Fig. 10a).

In the northern SCS alone, no apparent correlation is observed between SSB depth and average sedimentation rate (Fig. 10a). However, when the cores outside the mud areas, including the studied cores and others from the East China Seas, are considered together, SSB depth

Table 3

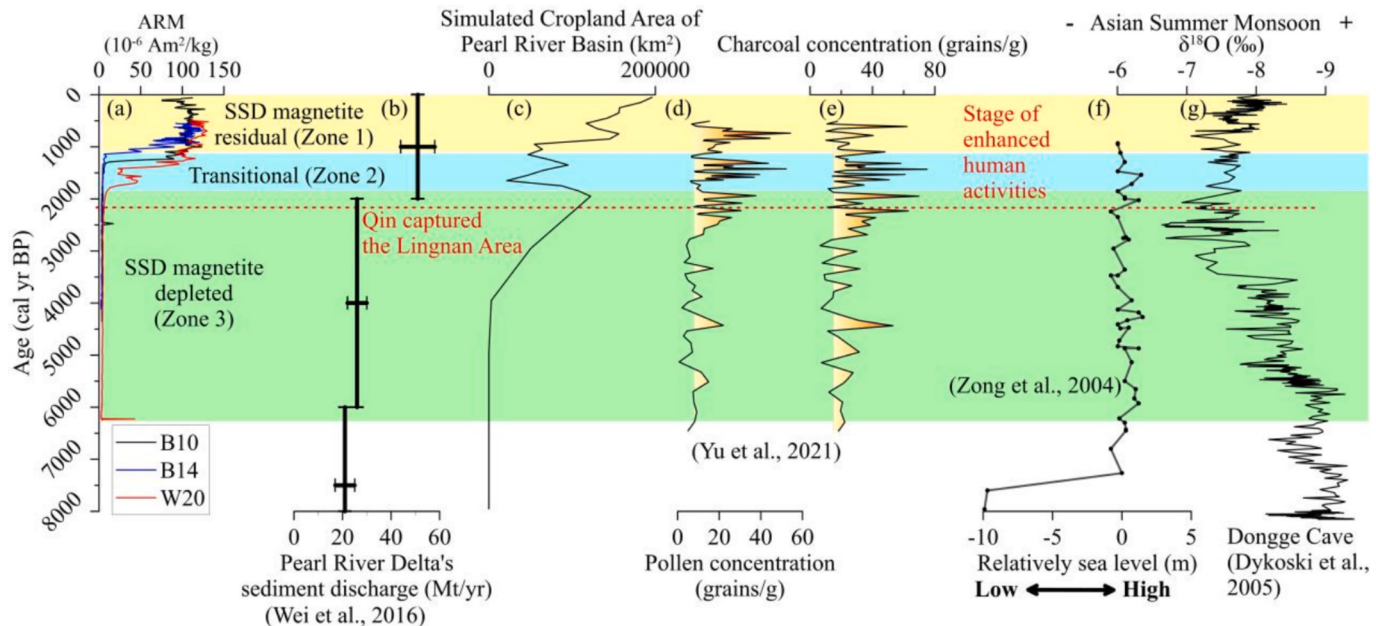
Comparisons of magnetic parameters in sediments from Zone 1 of cores B10, B14, and W20 with those from the northern SCS shelf.

Sample ID		χ_{lf} ($10^{-8} \text{ m}^3/\text{kg}$)	SIRM ($10^{-6} \text{ Am}^2/\text{kg}$)	ARM ($10^{-6} \text{ Am}^2/\text{kg}$)	χ_{fd} ($10^{-8} \text{ m}^3/\text{kg}$)	χ_{ARM}/χ_{lf}	SIRM/ χ_{lf} (kA/m)	S_{-300}	HIRM ($10^{-6} \text{ Am}^2/\text{kg}$)
W20	Mean	18.68	1816.04	119.87	1.85	16.12	9.74	0.80	182.96
	Max	20.19	1996.09	131.35	2.05	17.85	10.80	0.82	212.15
	Min	17.04	1631.04	107.25	1.39	14.78	9.12	0.77	165.46
B14	Mean	19.63	1857.21	110.64	2.92	14.15	9.47	0.80	183.09
	Max	20.69	2004.70	124.93	3.33	15.90	10.14	0.92	259.63
	Min	17.91	1521.34	90.19	2.55	11.93	8.02	0.73	60.11
B10	Mean	17.59	1675.70	104.69	1.77	15.02	9.55	0.81	158.57
	Max	19.92	1889.55	126.97	2.23	19.74	10.28	0.89	194.82
	Min	14.88	1484.45	75.73	1.32	10.78	8.17	0.79	87.94
North SCS shelf ^a	Mean	31.42	3072.20	127.38	1.68	11.70	9.95	0.82	258.50
	Max	110.05	10,803.70	206.24	6.11	16.35	10.79	0.87	711.90
	Min	4.49	455.30	22.03	0.17	4.71	8.47	0.73	41.60

^a Data from Region C of Li et al. (2024).**Fig. 10.** Scatter plots of depth to SSB vs. average sedimentation rate (a) and water depth (b). The data of East China seas are from (Cheng et al., 2020; Ge et al., 2015; Zheng et al., 2011).

shows a negative correlation with average sedimentation rates. Moreover, the depth to SSB and the slope of the relationship in Fig. 10a are lower for non-mud areas than for mud areas. This suggests two models with different slopes for the relationship between average sedimentation

rate and SSB depth in mud and non-mud regions. For paleoenvironmental reconstruction of river basins based on shelf cores, it is essential to seek the mineralogical, magnetic, and geochemical indicators unaffected by diagenesis. This updated model suggests that

**Fig. 11.** Comparisons of (a) ARM, (b) sediment discharge of the Pearl River Delta (Wei et al., 2016), (c) simulated cropland area of the Pearl River Basin extracted from HYDE3.2 (Goldewijk et al., 2017), (d) pollen concentration and (e) charcoal concentration recorded in core SCSF47, located close to W20 (Yu et al., 2021), (f) relatively sea level along the northern South China Sea coast (Zong, 2004), and (g) $\delta^{18}\text{O}$ values from a stalagmite Dongge cave, Pearl River Basin (Dykoski et al., 2005).

cores from mud areas with low sedimentation rates are the most suitable, as they preserve longer sedimentary records of environmental changes. However, limitations exist in this model. Because the age ranges of different core samples vary, the calculated average sedimentation rate may not reflect contemporaneous rates. To address this, new indicators are needed. Generally, in estuary-shelf systems, the average sedimentation rate correlates with water depth, as deeper regions receive less sediment and thus have lower rates. Comparison of SSB depth with water depth reveals negative correlations in both mud and non-mud regions (Fig. 10b). This diagram (Fig. 10b) may be used to estimate SSB depth and reconstruct the sedimentary history of source areas.

4.3. Possible anthropogenic constraints on magnetic mineral dissolution front

Few studies have linked down-core magnetic mineral dissolution to paleoclimate or environmental changes. Chang et al. (2016) revealed a lagged marine diagenetic record corresponding to fluctuations in the Asian monsoon. Our results show that the strong dissolution front (Zone 2b) consistently coincides with the onset of accelerated sedimentation rates and TOC (Figs. 4, 7). This suggests a potential link between rapid terrestrial sediment input and the position of the dissolution front. Similarly, Liu et al. (2021b) found that in a core from the East China Sea, rapid terrestrial sediment input caused the suboxic zone to become shallower due to anaerobic oxidation of methane, which facilitated the formation of HS⁻ and the conversion of iron oxides to iron sulfides. This suggests that rapid sediment accumulation may generally result in a shallower dissolution front on continental shelves.

In this study, the onset of accelerated sedimentation and the strong dissolution front occurred 1 to 2 ka ago, coinciding with the rapid filling period of the Pearl River Delta (Wei et al., 2016) (Fig. 11a-b). Both anthropogenic and natural factors must be considered. Globally, rapid infilling of major deltas since 1 to 2 ka BP has been attributed to anthropogenic soil erosion (Jenny et al., 2019). In southern China, after the Qin conquest of the Lingnan Area region around 2.2 ka BP, nearly one million people were relocated, leading to rapid regional development and expansion of cropland in the Pearl River Basin (Fig. 11c). Human activity was a major driver of the accelerated infill of the PRE (Wei et al., 2016; Xiong et al., 2020). Enhanced pollen and charcoal concentrations in core SCSF47 near the studied cores also reflect increased human activity (Fig. 11d-e) (Yu et al., 2021). From a natural perspective, over the past 2 ka, sea level has been relatively stable (Zong, 2004), and the Asian summer monsoon has been relatively weak (Dykoski et al., 2005) (Fig. 11f-g). These conditions are not conducive to significant sediment accumulation and cannot explain the rapid deposition observed. Furthermore, there are no significant hydrodynamic changes as indicated by grain size distributions (Fig. 2). This suggests that paleoclimatic changes were not the primary factors influencing sediment input, while intensified human activity likely led to rapid sediment accumulation and constrained the magnetic mineral dissolution front. Although a potential relationship between human activity and iron oxide dissolution is here, further core analyses are needed to determine whether this relationship is globally applicable. Given differences in sediment sources, climate, organic matter supply, and hydrodynamics among regions, future research should focus on analyzing additional cores to develop a detailed model of human-influenced magnetic mineral dissolution. Additionally, the resolution of our cores limits detailed stratigraphic analysis and interpretation.

5. Conclusion

Three cores from the northern SCS shelf were analyzed to examine mineral dissolution processes. Three main findings emerged. First, all cores consist uniformly of clayey silt and span the past 4 to 6 ka. Second, each core is divided into three sections: the suboxic surface layer (Zone

1), a magnetic transition layer with variable parameters (Zone 2), and a deeper layer showing strong dissolution (Zone 3). Magnetic minerals include magnetite and hematite, with signals indicating the presence of iron sulfides such as pyrite. This study discovered, for the first time, that the transition between Zones 2 and 3 corresponds to a rapid increase in accumulation rate. This timing coincides with the last 1 to 2 ka, a period of intensified human activity and increased terrestrial input of sediment and nutrients. These processes may have influenced magnetic mineral dissolution. However, further verification using additional cores is required.

CRediT authorship contribution statement

Mingkun Li: Methodology, Funding acquisition, Data curation, Conceptualization, Writing – original draft. **Meng Tang:** Project administration, Methodology, Investigation, Funding acquisition, Data curation. **Liang Chen:** Resources, Project administration, Methodology, Investigation, Data curation. **Yongying Zeng:** Methodology, Data curation. **Rou Wen:** Methodology, Data curation. **Junyu Lin:** Methodology, Data curation. **Mingjie Yu:** Supervision, Resources, Project administration, Data curation, Conceptualization, Writing – review & editing.

Declaration of competing interest

The authors declare the following financial interests/personal relationships which may be considered as potential competing interests:

Mingjie Yu reports financial support was provided by South China Normal University. Mingjie Yu reports a relationship with South China Normal University that includes: employment. If there are other authors, they declare that they have no known competing financial interests or personal relationships that could have appeared to influence the work reported in this paper.

Acknowledgments

This work was supported by the Guangdong Basic and Applied Basic Research Foundation, China (Grant No. 2019A1515110195; 2023A1515010675), Guangzhou Sci-Tech Intelligent Management Platform Project (Grant No. 2023A04J1992), Key Laboratory of Marine Environmental Survey Technology and Application, Ministry of Natural Resources (Grant No. MESTA-2023-A004), Science and Technology Development Foundation of South China Sea Bureau, Ministry of Natural Resources (Grant No. 240106), and Undergraduate Training Program on Innovation and Entrepreneurship (Grant No. 202526025). Thanks to Dr. Huang Chao of Guangdong Ocean University for his assistance in grain size testing. The authors also thank Bradák Balázs, and an anonymous reviewer for their insightful input which helped us to improve the final manuscript.

Appendix A. Supplementary data

Supplementary data to this article can be found online at <https://doi.org/10.1016/j.palaeo.2025.113263>.

Data availability statement

Data will be made available on request.

References

- An, Z., 2000. The history and variability of the East Asian paleomonsoon climate. *Quat. Sci. Rev.* 19, 171–187.
- Badesab, F., Dewangan, P., Gaikwad, V., Kars, M., Kocherla, M., Krishna, K.S., Sangode, S.J., Deenadayalan, K., Kumar, P., Naikgaonkar, O., 2019. Magnetic mineralogical approach for the exploration of gas hydrates in the Bay of Bengal. *J. Geophys. Res. Solid Earth* 124, 4428–4451.

- Berner, R.A., 1982. Burial of organic carbon and pyrite sulfur in the modern ocean; its geochemical and environmental significance. *Am. J. Sci.* 282 (4), 451–473.
- Blaauw, M., Christen, J.A., 2011. Flexible Paleoclimate Age-Depth Models Using an Autoregressive Gamma Process.
- Bloemendal, J., King, J., Hunt, A., Demenocal, P., Hayashida, A., 1993. Origin of the sedimentary magnetic record at ocean drilling program sites on the Owen Ridge, western Arabian Sea. *J. Geophys. Res.: Solid Earth* (1978–2012) 98 (B3), 4199–4219.
- Brachfeld, S., Domack, E., Kissel, C., Laj, C., Leventer, A., Ishman, S., Gilbert, R., Camerlenghi, A., Eglinton, I.B., 2003. Holocene history of the Larsen-A Ice Shelf constrained by geomagnetic paleointensity dating. *Geology* 31, 749–752.
- Canfield, D.E., Berner, R.A., 1987. Dissolution and pyritization of magnetite in anoxic marine sediments. *Geochim. Cosmochim. Acta* 51 (3), 645–659.
- Chang, L., Bolton, C.T., Dekkers, M.J., Hayashida, A., Heslop, D., Krijgsman, W., Kodama, K., Paterson, G.A., Roberts, A.P., Rohling, E.J., Yamamoto, Y., 2016. Asian monsoon modulation of nonsteady state diagenesis in hemipelagic marine sediments offshore of Japan. *Geochim. Geophys. Geosy.* 17 (11), 4383–4398.
- Chen, Y., Deng, B., Saito, Y., Wang, Z., Yang, X., Wu, J., 2023. Pearl River sediment dispersal over its associated delta-estuary-shelf system during the Holocene. *Sedimentology* 70 (70), 2331–2354.
- Cheng, Q., Wang, F., Chen, J., Ge, C., Zhao, X., Chen, Y., Nian, X., Zhang, W., Chen, Z., Liu, K., 2020. Spatial Variation of the magnetic properties from the Yangtze River subaqueous delta deposits and their implications for erosion/deposition study. *Acta Sedimentol. Sin.* 38 (6), 1215–1225 (in Chinese with English Abstract).
- Duan, Z., Liu, Q., Gai, C., Zhao, X., 2017. Magnetostratigraphic and environmental implications of greigite (Fe_3S_4) formation from Hole U1433A of the IODP Expedition 349, South China Sea. *Mar. Geol.* 394, 82–97.
- Dunlop, D.J., Özdemir, Ö., 2001. Rock Magnetism: Fundamentals and Frontiers. Cambridge University Press.
- Dykoski, C.A., Edwards, R.L., Cheng, H., Yuan, D., Cai, Y., Zhang, M., Lin, Y., Qing, J., An, Z., Revenaugh, J., 2005. A high-resolution, absolute-dated holocene and deglacial Asian monsoon record from Dongge Cave, China. *Earth Planet. Sci. Lett.* 233 (1–2), 71–86.
- Ellwood, B.B., Balsam, W.L., Roberts, H.H., 2006. Gulf of Mexico sediment sources and sediment transport trends from magnetic susceptibility measurements of surface samples. *Mar. Geol.* 230 (3), 237–248.
- Froelich, P.N., Klinkhamer, G.P., Bender, M.L., Luedtke, N.A., Heath, G.R., Cullen, D., Dauphin, P., Hammond, D., Hartman, B., Maynard, V., 1979. Early oxidation of organic matter in pelagic sediments of the eastern equatorial Atlantic: suboxic diagenesis. *Geochim. Cosmochim. Acta* 43 (7), 1075–1090.
- Ge, C., Zhang, W., Dong, C., Dong, Y., Bai, X., Liu, J., Hien, N.T.T., Feng, H., Yu, L., 2015. Magnetic mineral diagenesis in the river-dominated inner shelf of the East China Sea, China. *J. Geophys. Res. Solid Earth* 120 (7), 4720–4733.
- Ghilardi, M., Kunesch, S., Stylianou, M., Fouache, E.J.G., 2008. Reconstruction of Mid-Holocene sedimentary environments in the central part of the Thessaloniki Plain (Greece), based on microfaunal identification, magnetic susceptibility and grain-size analyses. *Geomorphology* 97 (3–4), 617–630.
- Goldewijk, K., Beusen, A., Doelman, J., Stehfest, E., 2017. Anthropogenic land use estimates for the Holocene-HYDE 3.2. *Earth Syst. Sci. Data* 9 (2), 927–953.
- Hanesch, M., Stanjek, H., Petersen, N., 2006. Thermomagnetic measurements of soil iron minerals—the role of organic carbon. *Geophys. J. Int.* 165 (1), 53–61.
- He, C., Ouyang, T., Li, M., Zhu, S., Yu, M., Peng, S., Zhu, Z., Wang, Y., Chen, H., Tian, C., 2024. Nonnegligible contribution of terrigenous sediment inputs from local small watersheds to west regions of the Pearl River Estuary, Northern South China Sea shelf. *Mar. Geol.* 107369.
- Hesse, P., Stoltz, J., 1999. Bacterial magnetite and the Quaternary climate record. *Quat. Clim., Env. Magn.* 390, 161–198.
- Hilgenfeldt, K., 2000. Diagenetic dissolution of biogenic magnetite in surface sediments of the Benguela upwelling system. *Int. J. Earth. Sci.* 88 (4), 630–640.
- Horng, C.-S., Torii, M., Shea, K.-S., Kao, S.-J., 1998. Inconsistent magnetic polarities between greigite- and pyrrhotite/magnetite-bearing marine sediments from the Tsailiao-chi section, southwestern Taiwan. *Earth Planet. Sci. Lett.* 164 (3), 467–481.
- Huang, C., Zeng, T., Ye, F., Xie, L., Wang, Z., Wei, G., Lo, L., Deng, W., Rao, Z., 2018. Natural and anthropogenic impacts on environmental changes over the past 7500 years based on the multi-proxy study of shelf sediments in the northern South China Sea. *Quat. Sci. Rev.* 197, 33–48.
- Huang, C., Kong, D., Chen, F., Hu, J., Wang, P., Lin, J., 2021. Multi-proxy reconstructions of climate change and human impacts over the past 7000 Years from an Archive of Continental Shelf Sediments off Eastern Hainan Island, China. *Front. Earth Sci.* 9.
- Jenny, J.-P., Koiralala, S., Gregory-Eaves, I., Francus, P., Niemann, C., Ahrens, B., Brovkin, V., Baud, A., Ojala, A.E., Normandeau, A., 2019. Human and climate global-scale imprint on sediment transfer during the Holocene. *Proc. Natl. Acad. Sci.* 116 (46), 22972–22976.
- Kao, S.-J., Horng, C.-S., Roberts, A.P., Liu, K.-K., 2004. Carbon-sulfur-iron relationships in sedimentary rocks from southwestern Taiwan: influence of geochemical environment on greigite and pyrrhotite formation. *Chem. Geol.* 203 (1), 153–168.
- Karlin, R., 1990. Magnetite diagenesis in marine sediments from the Oregon continental margin. *J. Geophys. Res. Solid Earth* 95 (B4), 4405–4419.
- Kim, W., Doh, S.-J., Yu, Y., Lee, Y.I., 2013. Magnetic evaluation of sediment provenance in the northern East China Sea using fuzzy c-means cluster analysis. *Mar. Geol.* 337, 9–19.
- Li, W., Hu, Z., Zhang, W., Ji, R., Nguyen, T.T.H., 2017. Influence of provenance and hydrodynamic sorting on the magnetic properties and geochemistry of sediments of the Oujiang River, China. *Mar. Geol.* 387, 1–11.
- Li, M., Zhu, S., Ouyang, T., Tang, J., He, C., 2020. Magnetic fingerprints of surface sediment in the Bohai Sea, China. *Mar. Geol.* 427, 106226.
- Li, M., Zhu, S., Ouyang, T., Tang, J., Tang, Z., 2021. Magnetic properties of the surface sediments in the Yellow River Estuary and Laizhou Bay, Bohai Sea, China: Implications for monitoring heavy metals. *J. Hazard. Mater.* 410, 124579.
- Li, M., Zeng, Y., Liu, S., Tang, M., Chen, L., Chen, J., Amorosi, A., Ouyang, T., 2024. Provenance and sediment dispersal in Pearl River Estuary, southern China unraveled by magnetic properties. *Mar. Geol.* 478, 107431.
- Liu, J., Chen, Z., Chen, M., Yan, W., Xiang, R., Tang, X., 2010. Magnetic susceptibility variations and provenance of surface sediments in the South China Sea. *Sediment. Geol.* 230 (1), 77–85.
- Liu, Y., Gao, S., Wang, Y., Yang, Y., Long, J., Zhang, Y., Wu, X., 2014. Distal mud deposits associated with the Pearl River over the northwestern continental shelf of the South China Sea. *Mar. Geol.* 347, 43–57.
- Liu, J., Shi, X., Liu, Q., Liu, S., Liu, Y., Zhang, Q., Yu, X., Fang, X., Wu, Y., Xu, T., 2021a. Authigenic iron sulphides indicate sea-level change on the continental shelf: An illustration from the East China Sea. *J. Geophys. Res. Solid Earth* p. e2020JB021222.
- Liu, X., Zhang, M., Li, A., Fan, D., Dong, J., Jiao, C., Chang, X., Gu, Y., Zhang, K., Wang, H., 2021b. Depositional control on carbon and sulfur preservation onshore and offshore the Oujiang Estuary: Implications for the C/S ratio as a salinity indicator. *Cont. Shelf Res.* 227, 104510.
- Maher, B.A., 2007. Environmental magnetism and climate change. *Contemp. Phys.* 48, 247–274.
- Maher, B.A., Thompson, R., 1999. Quaternary Climates, Environments and Magnetism. Cambridge University Press.
- Mohamed, K.J., Rey, D., Rubio, B., Dekkers, M.J., Roberts, A.P., Vilas, F., 2011. Onshore-offshore gradient in reductive early diagenesis in coastal marine sediments of the Ria de Vigo, Northwest Iberian Peninsula. *Cont. Shelf Res.* 31 (5), 433–447.
- Oldfield, F., 1991. Environmental magnetism—a personal perspective. *Quat. Sci. Rev.* 10 (1), 73–85.
- Ouyang, T., Appel, E., Jia, G., Huang, N., Zhu, Z., 2013. Magnetic mineralogy and its implication of contemporary coastal sediments from South China. *Environ. Earth Sci.* 68 (6), 1609–1617.
- Ouyang, T., Li, M., Appel, E., Fu, S., Jia, G., Li, W., Zhu, Z., 2017. Magnetic properties of surface sediments from the Pearl River Estuary and its adjacent waters: Implication for provenance. *Mar. Geol.* 390, 80–88.
- Passier, H., De Lange, G., Dekkers, M., 2001. Magnetic properties and geochemistry of the active oxidation front and the youngest sapropel in the eastern Mediterranean Sea. *Geophys. J. Int.* 145 (3), 604–614.
- Roberts, A.P., 2015. Magnetic mineral diagenesis. *Earth Sci. Rev.* 151, 1–47.
- Roberts, A.P., Turner, G.M., 1993. Diagenetic formation of ferrimagnetic iron sulphide minerals in rapidly deposited marine sediments, South Island, New Zealand. *Earth Planet. Sci. Lett.* 115 (1), 257–273.
- Rowan, C.J., Roberts, A.P., Broadbent, T., 2009. Reductive diagenesis, magnetite dissolution, greigite growth and paleomagnetic smoothing in marine sediments: a new view. *Earth Planet. Sci. Lett.* 277 (1), 223–235.
- Simkins, L.M., Simms, A.R., Cruse, A.M., Troiani, T., Atekwana, E.A., Puckette, J., Yokoyama, Y., 2012. Correlation of early and mid-Holocene events using magnetic susceptibility in estuarine cores from bays along the northwestern Gulf of Mexico. *Palaeogeogr. Palaeoclimatol. Palaeoecol.* 346, 95–107.
- Stephenson, A., 1971. Single domain grain distributions II. The distribution of single domain iron grains in Apollo 11 lunar dust. *Phys. Earth Planet. Inter.* 4 (5), 361–369.
- Svitiksi, J., Ángel, J.R., Saito, Y., Overeem, I., Vörösmarty, C.J., Wang, H., Olago, D., 2022. Earth's sediment cycle during the Anthropocene. *Nat. Rev. Earth Environ.* 3 (3), 179–196.
- Vigliotti, L., Verosub, K., Cattaneo, A., Trincardi, F., Ascoli, A., Piva, A., 2008. Palaeomagnetic and rock magnetic analysis of Holocene deposits from the Adriatic Sea: detecting and dating short-term fluctuations in sediment supply. *The Holocene* 18 (1), 141–152.
- Wang, Y., Yu, Z., Li, G., Oguchi, T., He, H., Shen, H., 2009. Discrimination in magnetic properties of different-sized sediments from the Changjiang and Huanghe Estuaries of China and its implication for provenance of sediment on the shelf. *Mar. Geol.* 260 (1), 121–129.
- Wang, Z., Li, M., Zhang, R., Zhuang, C., Liu, Y., Saito, Y., Xie, J., Zhao, B., 2011. Impacts of human activity on the late-Holocene development of the subaqueous Yangtze delta, China, as shown by magnetic properties and sediment accumulation rates. *The Holocene* 21 (3), 393–407.
- Wang, Y., Jiao, J.J., Zhang, K., Zhou, Y., 2016. Enrichment and mechanisms of heavy metal mobility in a coastal quaternary groundwater system of the Pearl River Delta, China. *Sci. Total Environ.* 545, 493–502.
- Wang, Y., Wang, S., Liu, M., 2017. Magnetic properties indicate sediment provenance and distribution patterns in the Bohai and Yellow Seas, China. *Cont. Shelf Res.* 140, 84–95.
- Wang, S., Liu, J., Li, J., Xu, G., Qiu, J., Chen, B., 2020. Environmental magnetic parameter characteristics as indicators of heavy metal pollution in the surface sediments off the Zhoushan Islands in the East China Sea. *Mar. Pollut. Bull.* 218, 108–117.
- Wang, X., Wang, L., Hu, S., Meng, L., Zeng, L., Cui, B., Zhan, C., Liu, X., Wang, K., 2022. Magnetic responses for heavy-metal pollution recorded by the sediments from Bohai Sea, Eastern China. *iScience* 25, 105280.
- Wang, Y., Chen, X., Switzer, A., Li, L., Xu, Y., Wang, Y., Zhang, P., 2023. Relict and Modern Sediments on the Continental Shelf of the Northern South China Sea: a reconsideration. *J. Geophys. Res. Earth* 128.
- Wang, F., Huang, T., Wang, Z., Zhang, W., Qiao, P., Tang, H., Mei, X., Yin, P., Lai, Z., 2025. Magnetic evidence of redox transition event in the Okinawa Trough during the

- early-middle Holocene and its links to the Kuroshio current evolution. *Glob. Planet. Chang.* 245, 104699.
- Wei, X., Wu, C., Ni, P., Mo, W., 2016. Holocene delta evolution and sediment flux of the Pearl River, southern China. *J. Quaternary. Sci.* 31 (5), 484–494.
- Wu, Y., Cai, G., Li, S., Wang, S., Fu, S., Han, Y., Tao, S., 2024. Characterizing holocene environmental transitions using magnetic properties of sediments from the continental shelf of the Northern South China Sea. *Mar. Geol.* 107464.
- Xiong, H., Zong, Y., Huang, G., Fu, S., 2020. Human drivers accelerated the advance of Pearl River deltaic shoreline in the past 7500 years. *Quat. Sci. Rev.* 246, 106545.
- Xue, P., Chang, L., Wang, S., Liu, S., Li, J., Shi, X., Khokattiwong, S., Kornkanitnan, N., 2019. Magnetic mineral tracing of sediment provenance in the Central Bengal Fan. *Mar. Geol.* 415, 105955.
- Yang, X., Heller, F., Wu, N., Yang, J., Su, Z., 2009. Geomagnetic paleointensity dating of South China Sea sediments for the last 130 kyr. *Earth Planet. Sci. Lett.* 284, 258–266.
- Yim, W.-S., Huang, G., Chan, L., 2004. Magnetic susceptibility study of late quaternary inner continental shelf sediments in the Hong Kong SAR, China. *Quat. Int.* 117 (1), 41–54.
- Yu, S., Chen, F., Jing, X., Chen, C., Zhuang, C., Li, Q., Zhou, Y., Xia, Z., Gan, H., Fisch, K., Waniek, J.J., 2021. Increasing terrigenous pollen input in the late Holocene: Indications of intensive human activity and accelerated delta plain progradation. *Mar. Geol.* 439, 106547.
- Zhao, J., Zhang, L., Yongdong, Z., Yu, Q., Luo, S., 2024. Lipid biomarker evidences of natural and anthropogenic organic matter inputs in sediments from the eastern Sunda Shelf in the southern South China Sea. *Cont. Shelf Res.* 275, 105184.
- Zheng, Y., Kissel, C., Zheng, H.B., Laj, C., Wang, K., 2010. Sedimentation on the inner shelf of the East China Sea: magnetic properties, diagenesis and paleoclimate implications. *Mar. Geol.* 268, 34–42.
- Zheng, Y., Zheng, H., Kissel, C., Laj, C., 2011. Sedimentation rate control on diagenesis, East China Sea sediments. *Phys. Earth Planet. Inter.* 187 (3), 301–309.
- Zhong, Y., Chen, Z., Li, L., Liu, J., Li, G., Zheng, X., Wang, S., Mo, A., 2017. Bottom water hydrodynamic provinces and transport patterns of the northern South China Sea: evidence from grain size of the terrigenous sediments. *Cont. Shelf Res.* 140, 11–26.
- Zong, Y., 2004. Mid-Holocene Sea-level highstand along the Southeast Coast of China. *Quat. Int.* 117 (1), 55–67.
- Zong, Y., Huang, G., Switzer, A., Yu, F., Yim, W.-S., 2009. An evolutionary model for the Holocene formation of the Pearl River delta, China. *The Holocene* 19 (1), 129–142.
- Zong, Y., Yu, F., Huang, G., Lloyd, J.M., Yim, W.W.S., 2010. Sedimentary evidence of late Holocene human activity in the Pearl River delta, China. *Earth Surf. Process. Landf.* 35 (9), 1095–1102.